Multi-stage heterogeneous bubble nucleation under negative pressures

Anirban Chandra,[1] Harrison Lee,[2] Shekhar Garde,[3] and Pawel Keblinski[2, a)]

[1)]*Department of Mechanical, Aerospace, and Nuclear Engineering, Rensselaer Polytechnic Institute, Troy, New York 12180, USA*

[2)]*Department of Materials Science and Engineering, Rensselaer Polytechnic Institute, Troy, New York 12180, USA*

[3)]*Department of Chemical and Biological Engineering, Rensselaer Polytechnic Institute, Troy, New York 12180, USA*

In this paper, we investigate homogeneous and heterogeneous bubble nucleation processes in systems under tension using molecular dynamics simulations. The maximum pressure (nucleation pressure, σ_{min}) sustained by the system is used a as measure of the system's propensity to nucleate a vapor bubble. In the presence of a planar gold substrate, nucleation pressure is essentially the same as homogeneous values when strong interaction exists between the gold atoms and water molecules; at weaker interactions, a significant lowering of nucleation pressure is observed, signifying that nucleation from such surfaces is easier. Reduction in nucleation pressure with decreasing gold-water surface interaction strength obtained from our simulations shows a good qualitative agreement with classical heterogeneous nucleation theory. As compared to planar surfaces, surfaces with grooves show a further reduction in nucleation barrier only for weak interfacial interactions. Furthermore, the groove dimensions also influence σ_{min} – an optimal groove geometry exists for which σ_{min} is minimized; our results indicate that this occurs when the length scale of the defect is comparable to that of the critical (homogeneous) bubble nucleation radius. Moreover, in the presence of defects, multiple barriers to nucleation exist. Our findings provide design guidelines for surface grooves for controllable generation of vapor bubbles; such hydrophobic grooves should be avoided for maximizing overheat or can be used for spatially controlled boiling.

[a)]Electronic mail: keblip@rpi.edu

I. INTRODUCTION

Two-phase cooling facilitated by liquid-to-vapor phase change allows for a high rate of heat extraction due to the large latent heat associated with intermolecular interactions. Consequently, evaporative cooling is used in applications involving large heat fluxes, such as in thermal management of nuclear plants[1] and high power electronic devices[2,3]. Evaporation-driven processes are also widely used to generate clean water[4], electricity production[5] and high temperature steam sterilization[6,7]. Recently, steam sterilization has been shown to be particularly instrumental in disinfecting disposable masks and extending its usability for the fight against COVID-19[8,9]. Another promising application of evaporation is in the utilization of solar energy. In the last decade, solar-driven interfacial evaporation technologies have gained tremendous interest due to boost in energy conversion efficiencies facilitated by innovation in photo-thermal materials and interfacial heat localization strategies[10–13].

Despite decades of investigations on evaporation/condensation based thermal transport processes, non-equilibrium regimes are still poorly understood and have been the subject of various theoretical[14], experimental[15], and numerical[16–24] investigations due to potential applications in microscale devices and novel technologies. Specifically, the process of initial vapor bubble nucleation, which is an important aspect in understanding two-phase cooling phenomena, has remained primarily a black box and is often described by a set of fitting parameters[25,26]. Vapor bubble formation in water typically occurs either by cavitation (through pressure reduction) or boiling (by increasing temperature). Experimental investigations have shown that the bubble typically nucleates at much lower values of pressures and temperatures than what is predicted by classical nucleation theory[27]. Rationalization of this observation has involved consideration of surface defects, floating particles, and entrapped gases or bubbles[28]. Although cavitation in simple liquids has been studied extensively using computer simulations[29–31], limited investigations have been performed at state points away from the vapor-liquid spinodal[32] and on heterogeneous systems[33,34].

Boiling, a type of two phase heat transfer process, has been widely utilized across various industrial applications. The key performance parameter which determines the heat removal in boiling is the critical heat flux (CHF), i.e., the heat flux at which a liquid is dried out from a hot solid surface. The formation of a vapor film envelopes the heated surface and leads to an uncontrollable temperature rise and subsequent device failure[35]. The maximization of CHF is a complex problem that involves nucleation, boiling, and bubble departure. Moreover, there exists

an optimal point where the contact line region (where liquid, vapor, and solid phases meet) is maximal (leading to the highest possible evaporation rate), but not large enough for instabilities to cause a dry-out. In practice, the CHF is $\sim 100 W/cm^2$[36] and even with significant efforts involving nano/micro-structured surfaces[37–39], CHF in pool boiling experiments improved by factor of 2-3 over its nominal value[36,40]. Surprisingly, theoretical limit of evaporative cooling is in the order of $10 kW/cm^2$[41]. Understanding the bubble nucleation processes from surfaces/defects would shed light on the cause of this deviation.

While theory and simulation are significantly simpler for homogeneous nucleation, in most practical situations, heterogeneous nucleation is perhaps the only practically relevant nucleation mechanism. Heterogeneous nucleation process is sensitive to liquid-solid surface interactions, presence of surface cavities/crevices and pockets of pre-existing gases. Due to this complexity our current understanding of heterogeneous nucleation it is mostly phenomenological in nature. Molecular dynamics (MD) simulations are an excellent tool for developing both fundamental microscopic understanding and quantitative predictions of many key aspects of heterogeneous nucleation. However, MD simulations of vapor bubble nucleation are challenging, due to very large nucleation barriers and small nucleation rates. Consequently, direct MD simulations of vapor nucleation are mainly limited to rapid heating, e.g., by a hot solid surface that brings the liquid close or to the spinodal line, where the nucleation barrier becomes zero. Such studies were performed for flat surfaces[42,43] and around nanoparticles[44]. While they can shed light on rapid laser heating induced vapor formation, the kinetics of this highly thermally driven and non-equilibrium process has little relevance to standard nucleation processes. In particular, it was observed that rapid heating of hydrophilic surfaces enables vapor formation, while hydrophobic surfaces are less effective in this respect[43]. This behavior is completely opposite to what has been observed experimentally in "close to equilibrium" nucleation processes that are promoted by lower nucleation barriers present on weakly wetting surfaces[45]. The likely reason for the behavior observed in aforementioned studies is that during rapid heating by hot solid hydrophilic surface, the rate of temperature increase of the liquid is faster due to lower interfacial thermal resistance. This effect is not present near equilibrium, when solid and liquids are at almost the same temperature regardless of the interfacial wetting properties.

More relevant to the actual nucleation process are MD simulations where vapor nucleation is induced by increasing simulation cell volume, and thus, applying negative pressure or tension to the liquid phase. Under tension, the nucleation barrier is lower and the critical radius is smaller,

which allows a direct observation of vapor bubble formation by MD simulations[46,47]. In fact, it was demonstrated for simple liquids described by Lennard-Jones potential that, with this approach, it is possible to observe vapor nanocavity formation and characterize cavity growth rate that exhibits large deviation from the rate predicted by continuum theory[47].

In this paper, using systems under tension we investigate the bubble nucleation mechanisms from flat surfaces with grooves. The maximum pressure sustained by the system (nucleation pressure) is used as a surrogate to understand the propensity to nucleate. Homogeneous nucleation studies are carried out to set a reference point for our heterogeneous simulations. The remainder of the paper is structured as follows. In Section 2 we present our modeling methodology and simulation details. Section 3 details our results. Finally, in Section 4 we summarize our findings.

II. METHODS

All our simulations are performed using the open-source molecular dynamics code LAMMPS[48], and visualized in OVITO[49]. Our systems consist of either pure water or water with an embedded slab of gold. Interaction potential between these components, an important input to all classical MD simulations, is delineated in Section II A. There are two kinds of simulations performed in this work: (a) Contact angle calculation (b) Non equilibrium molecular dynamics (NEMD) straining; detailed description of these are presented later in this Section. A constant time step size is 2fs is used across all our simulations.

A. Interatomic interaction potential

Intermolecular interaction between water molecules is described by the standard SPC/E[50] potential. However, the coulombic terms are evaluated using the Wolf summation technique[51,52] with a damping factor of 0.12Å^{-1}. A cutoff of 10Å is used for both Lennard Jones and coulombic interactions. This specific potential form was previously used and verified in our earlier study on interfacial liquid-vapor phase change[18]. Bond lengths and angle of the water molecules are constrained using the Shake algorithm[53]. Interaction between the gold atoms are modeled using the Embedded-atom potential[54].

The 12-6 Lennard Jones potential is used to describe the interaction between gold atoms and water molecules. While $\sigma_{Au-O}(= 3.6\text{Å})$ is consistent with prior literature[55], ε_{Au-O} is used as ad-

justable parameter to achieve different wetting conditions. Interactions between water hydrogens and gold atoms are not present. This specific gold-water interaction potential was tailored by Merabia *et al.*[55] to match the experimental wetting contact angle at 300K. ε_{Au-O} used in their study was 0.0256eV. Since our simulations are performed at 370K, we observe a transition from partial to complete wetting at lower value of ε_{Au-O}. To span both hydrophilic and hydrophobic conditions ε_{Au-O} is selected from the set – {0.0128, 0.0112, 0.0096, 0.0080, 0.0064}eV. Even with the highest value of ε_{Au-O} used in this study, we obtain a finite contact angle (see Figure 5). Going forward, for ease of representation, a non-dimensional notation for ε_{Au-O} is employed. ε^* denotes the value of ε_{Au-O} after normalizing it with 0.0128eV; therefore, $\varepsilon^* = 1$ denotes the strongest and $\varepsilon^* = 0.5$ the least wetting scenarios.

B. Non-equilibrium molecular dynamics (NEMD) simulations of straining: Systems under tension

Our approach for investigating the bubble nucleation process involves reduction of the nucleation barrier by applying negative pressures on the system. Under such conditions, the nucleus size is small enough that the entire process can be observed in ∼nm scale simulation geometries. However, to mimic bulk-like behavior periodic boundary conditions are applied in all three directions. For studying homogeneous (water) nucleation, initial equilibration is carried out on a cubical system using isotropic NPT integration scheme[56–59] at 1atm and 370K for 200ps; this equililibration time is chosen such that the systematic variations in macroscopic variables, like density, are nullified. Box dimensions obtained after equilibrated are shown in the first row of Table I.

The equilibration process for creating heterogeneous (water+gold slab) systems needs more careful considerations as residual stresses are undesirable. A gold slab that spans the simulation box in the x & y directions, and has a thickness of $\sim$ 24.5Å (6 unit cells of FCC gold with lattice parameter of 4.08Å) is created and equilibrated using anisotropic NPT (pressure control in x, y, and z directions are uncoupled) integration scheme at 1atm and 370K. Subsequently, the simulation box size in the z direction is increased and water molecules are introduced in the empty space created. Gold atoms are removed to carve out nano-grooves in specific cases (see Section III C). Then anisotropic NPT equilibration at 370K and 1atm is carried out. Box dimensions obtained after equilibration are reported in Table I.

	(L_x, L_y, L_z)	Num. of Water molecules
Homogeneous	∼(66Å, 66Å, 66Å)	9009
Heterogeneous (small)	∼(65Å, 65Å, 97Å)	9066
Heterogeneous (large)	∼(113Å, 65Å, 101Å)	16554

TABLE I: Equilibrated simulation box sizes.

Irrespective of the case being studied, homogeneous or heterogeneous, the procedure for straining the system is identical. A schematic of the heterogeneous nucleation straining simulation setup is shown in Figure 1; the homogeneous setup is similar with the exceptions: gold slab is absent and $L_x = L_y = L_z$. After initial equilibration, we impose a uniform strain in z-direction. Each straining simulation has a duration of 2ns, during which z-dimension of the box changes by 15%. L_z, simulation box length in the z direction, is changed every 20fs while performing NVT[60,61] thermostating every timestep. Normal stress, σ_{zz} is monitored and used to explicate the nucleation phenomena. Henceforth, σ_{zz} is interchangeably referred to as pressure, and has a non-positive value as our system is under tension. To obtain reasonable estimates of σ_{zz}, for each case at least 5 (maximum 10) independent simulations are performed.

An important parameter which influences the heterogeneous bubble nucleation process is the contact angle, θ. Later, in Section III B, we describe how θ varies with ε^* and its implications on the nucleation process. However, in the next Subsection, the simulation procedure for evaluation of θ is discussed.

C. Determination of contact angle

These simulations are performed in a cubodial box of dimensions (x – 293.76Å, y – 293.76Å, z – 204Å) with periodic boundary conditions applied in all three directions. The simulation cell consists of a gold slab (thin sheet) wherein the atoms are organized in a FCC lattice with a spacing of 4.08Å. The slab spans x & y box dimensions and has a thickness of ∼ 24.5Å. In the initial state 4435 water molecules are placed near the slab. To evolve the system, Nosé-Hoover thermostatting[62,63] at 370K is performed separately on the water and gold atoms. After ∼200ps of equilibration, a droplet is formed on the gold surface with a contact angle that varies with the specified ε_{Au-O}. Following the equilibration process, several snapshots of the system are utilized

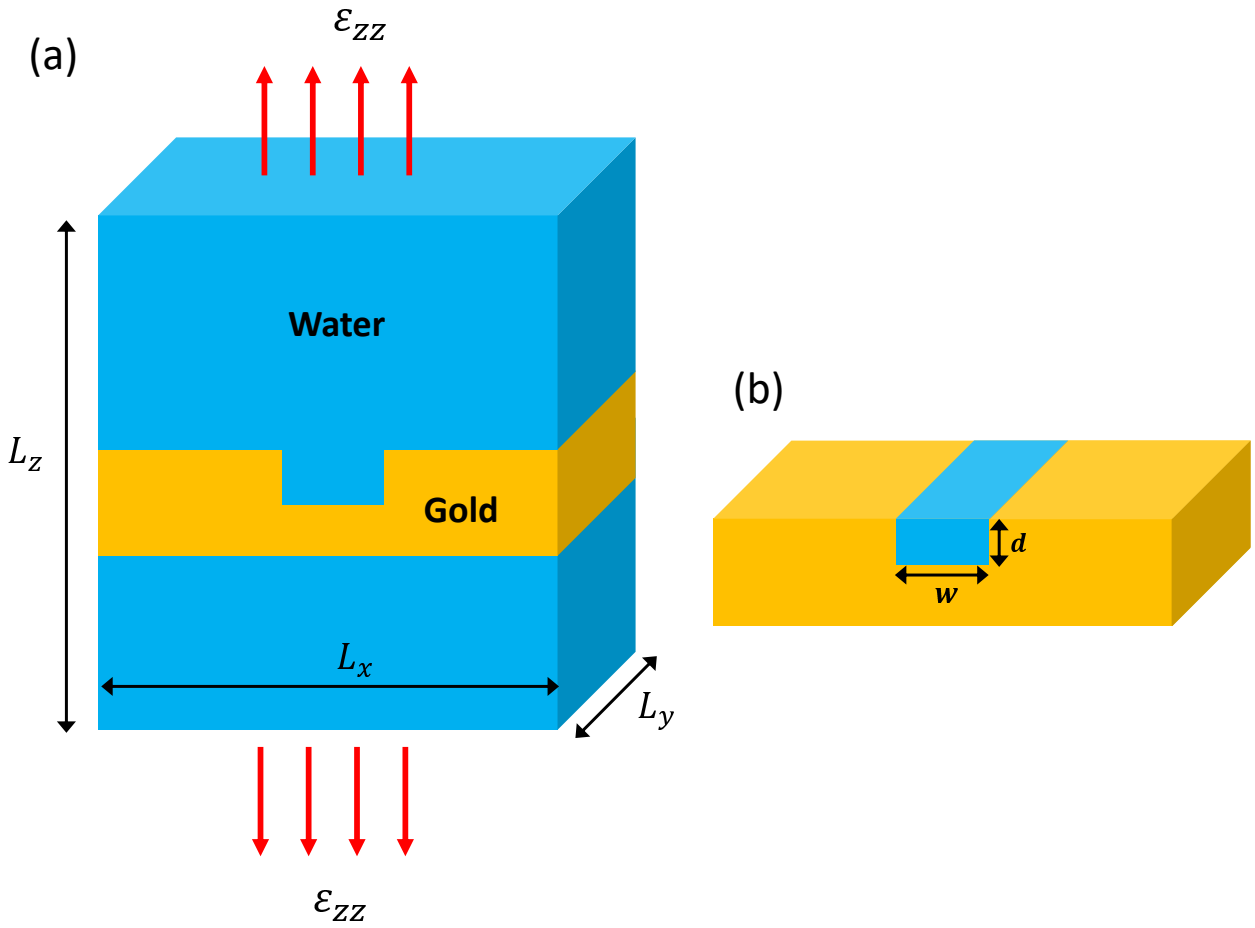

FIG. 1: (a) Schematic of heterogeneous (from grooves) nucleation simulation setup. ε_{zz} denotes the uniform strain applied along the z axis. Periodic BCs are used in all directions. (b) Zoomed-in view of the gold slab with an etched groove.

to evaluate the contact angle as described next.

Figure 2 shows the schematic of a liquid droplet with radius, R and contact angle, θ. Using these two independent parameters, expressions for volume and base area of the liquid droplet can be obtained: $V = \frac{1}{3}\pi R^3(1-\cos\theta)^2(2+\cos\theta)$ and $A = \pi R^2 \sin^2\theta$. Water molecules exclusively in the liquid phase (droplet) are determined by coordination number (> 8) of oxygen atom; hydrogen atoms are not considered in the coordination analysis. A cutoff of $\sim 2\sigma_{O-O}$ is used for obtaining the coordination number of each oxygen. The identified water molecules are then treated as data points for creating convex hull using the boundary function in MATLAB ver. R2020a; this procedure gives an estimate of the droplet volume, V. Similarly, the base area, A, is estimated by considering oxygen atoms lying within $\sim 2\sigma_{O-O}$ of the gold surface, projecting it onto the x-y plane, and then calculating area of the polygon which encompasses the projected points. There-

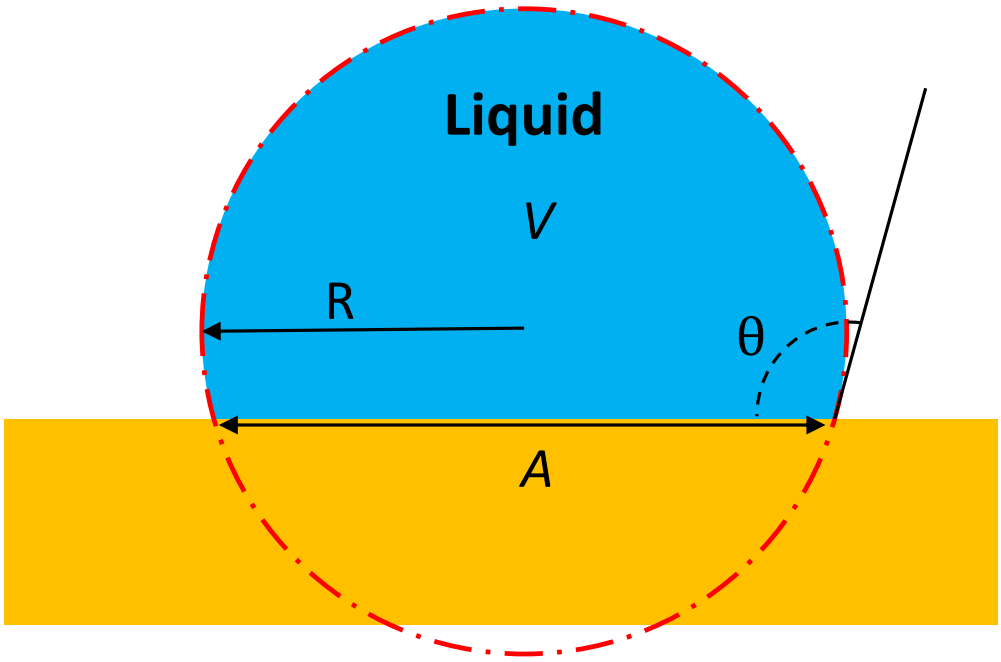

FIG. 2: Slice view (2D schematic) of liquid droplet on a gold substrate. The droplet is assumed to be a part of a sphere, denoted by red dash-dot line . 'A' denotes the contact area between the droplet and substrate, 'V' the volume of droplet, and θ the contact angle.

fore, expressions for V and A yield a system of non-linear equations, with θ and R as independent variables; θ is obtained after solving these equations. It should be noted that there are more sophisticated methods for determining the contact angles[64]. In this work, we focus on capturing the qualitative trends in variation of contact angle rather that obtaining precise quantitative estimates. Therefore, investigations in such directions are not undertaken.

III. RESULTS AND DISCUSSION

A. Homogeneous bubble nucleation

We first study homogeneous nucleation to establish a reference for our heterogeneous simulations. The procedure for generation of a stable bubble nuclei using NEMD is described in Section II B. Figure 3 portrays the homogeneous nucleation process. The gray shaded area denotes the surface of the bubble. Red and blue colored atoms denote oxygen and hydrogen respectively. Visualization settings are chosen such that only atoms near surfaces (which are selected based on a coordination number analysis) are visible while the remainder are semi-transparent. Until $\sim 1400 ps$,

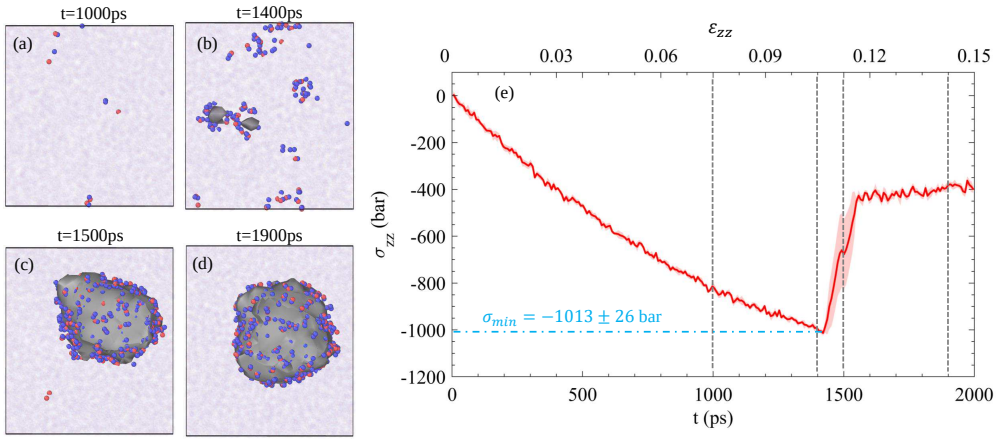

FIG. 3: Homogeneous bubble nucleation. (a)-(d): Snapshots of the system at different time instants where the shaded area denotes the bubble nucleus (e): Pressure variation as a function of time (bottom axis) and strain (top axis). The vertical dashed lines denote the different time instants shown in panels (a)-(d).

the pressure reduces (becomes negative) with increasing strain and the liquid is in superheated regime. During this time, several bubble nuclei are formed but collapses as the radii is not above the critical radius at the corresponding pressure; these small transient bubbles can be observed in Figure 3(b). At $t = 1500ps$, the first stable bubble nuclei is formed and subsequently grows as the system is further strained. On the pressure-time plot, the nucleation process is characterized by a rapid increase in pressure (relaxation of the stress) between $t = 1450ps$ and $t = 1550ps$. After a stable bubble is nucleated, it enters the growth regime which is evidenced by a slow relaxation of pressure with increasing strain; this can be observed in 3(e) after $t = 1550ps$. Maximum negative pressure sustained by the system is $1013 \pm 26bar$ which is comparable to those predicted from theory[65,66], experiments[67], and simulations[68]. Critical bubble nuclei radius calculated from our simulations is $\sim$10Å, as discussed in Supplementary Section I.

B. Heterogenous nucleation from atomistically flat surfaces

The simplest form of heterogeneous nucleation occurs from flat surfaces, although in reality it is extremely improbable due to the presence of cracks/crevices on macroscopic surfaces. Nevertheless, in this Section, we focus on atomistically flat surfaces to set a reference point for more realistic systems studied in Section III C. When the interaction between gold slab and water molecules is strong, i.e., $\varepsilon^* = 1$, nucleation occurs in the bulk liquid (see Figure 4(a)), similar

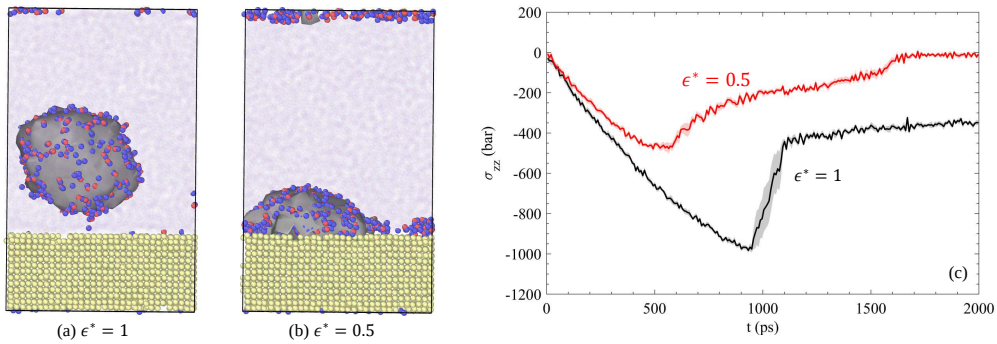

FIG. 4: Heterogeneous bubble nucleation from flat surfaces. (a)-(b): Snapshots of the system for different surface interactions after a stable bubble nucleates (c): Pressure variation as a function of time for two limiting surface interactions.

to the homogeneous system. Minimum pressure (σ_{min}) sustained, denoted by black solid lines in Figure 4(c), is comparable to that obtained from our prior homogeneous simulations. On the contrary, when $\varepsilon^* = 0.5$, nucleation occurs at the interface, as shown in Figure 4(b). Pressure-time curves also corroborate this finding – minimum pressure sustained by the system is significantly larger than $\sigma_{min,bulk}$.

Classical heterogeneous nucleation theory predicts[69] that the ratio of free energies for heterogeneous and homogeneous is a function, Γ, which depends solely on the contact angle of the nucleated bubble. Γ takes the form,

$$\Gamma = \frac{\Delta G_{hetero}}{\Delta G_{homo}} = \frac{(1+\cos\theta)^2(2-\cos\theta)}{4}. \tag{1}$$

Estimating the contact angle (θ) from negative pressure simulations are challenging as these are performed in highly non-equilibrium conditions and the bubble dimensions change constantly. Therefore, we revert to the standard method of determining contact angles wherein a liquid droplet is placed on a solid substrate. Simulation setup and details are presented in Section II C. Figure 5 shows the contact angle variation of a liquid droplet with ε^*. The most wetting scenario yields a non-zero contact angle of about 30^o while the least wetting case is mildly hydrophobic with $\theta \sim 110^o$. Furthermore, consistent with prior studies[70], we observe an increase in contact angle with decreasing droplet sizes. Our choices of ε^* thus enable us to monitor both hydrophilic and hydrophobic regimes.

σ_{min} for intermediate ε^* values, between 0.5 and 1 is shown in Figure 6(a). σ_{min} decreases monotonically with ε^* till $\varepsilon^* = 0.875$ and stagnates at the bulk value. $\varepsilon^* = 0.875$ acts a transition

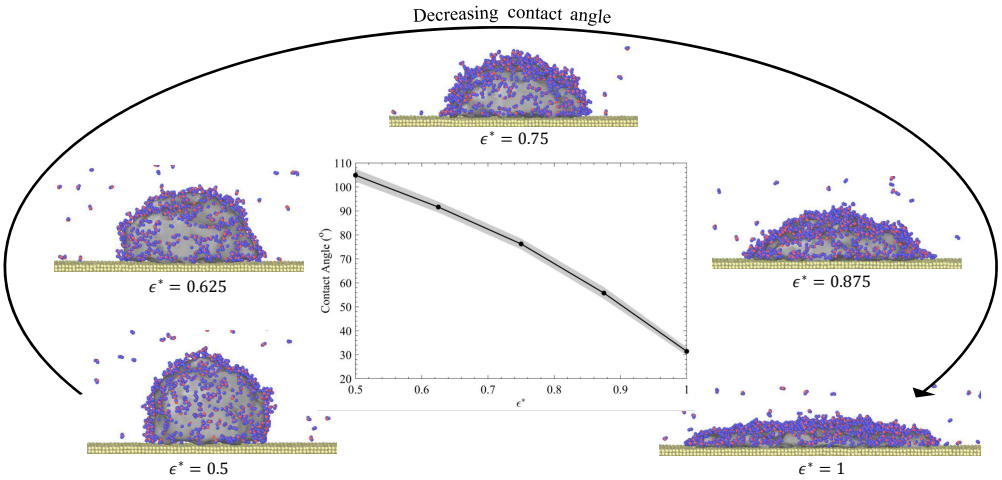

FIG. 5: Contact angle of a liquid droplet on a gold substrate. The gray shaded area denotes the liquid droplet.

point between heterogeneous and homogeneous nucleation which is evidenced by the fact that, out of all the independent simulations considered for this specific ε^*, the ratio of nucleation events occurring in the bulk to interface is ~ 0.5. For higher (lower) wetting situations, the bubble forms solely inside the liquid (at interface). The ratio of nucleation pressure for different interfacial interactions, σ_{min}, to $\sigma_{min,bulk}$ represents a non-dimensional factor which partially resembles Γ introduced in Equation 1. We show the variation of this factor on the left axis of Figure 6(b). Simultaneously, on the right axis, using contact angles values obtained from Figure 5, we estimate Γ. Despite minor quantitative differences, a good qualitative match is observed – as interfacial interactions becomes weaker the nucleation barrier reduces. We attribute the minor deviation in behavior of Γ and $\frac{\sigma_{min}}{\sigma_{min,bulk}}$ between $\varepsilon^* = 0.875$ and $\varepsilon^* = 1.0$ to the fundamental description of these two parameters: Γ is based on thermodynamic considerations while the pressure ratio is a purely mechanical quantity. More rigorous investigations are necessary to ascertain the exact cause of this quantitative deviation.

C. Heterogeneous nucleation from surface defects

As discussed in the previous Subsection, the magnitude of nucleation pressure reduced (in general) with decreasing interaction strength between the surface and water molecules. To further explore the implications of this observation, here we first investigate the effect on changing ε^* on a surface with a groove (defect). Subsequently, we study the effect of nucleation pressure on groove

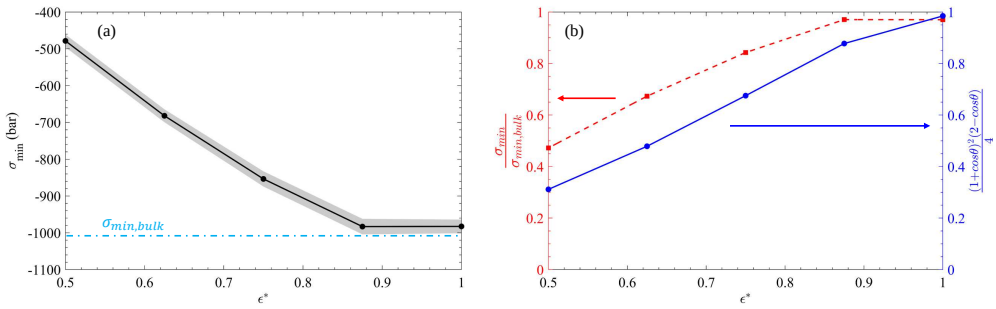

FIG. 6: Effect of interfacial interactions (ε^*) on heterogeneous bubble nucleation from atomistically flat surfaces. (a): Nucleation pressure as a function of interfacial interaction strength (b): Variation of $\Gamma = \frac{(1+\cos\theta)^2(2-\cos\theta)}{4}$ and $\frac{\sigma_{min}}{\sigma_{min,bulk}}$ with interfacial interactions.

width and depth. Methodology for creation of nanogrooves and simulation procedure is described in Section II B.

1. *Effect of gold-water interfacial interactions (ε^*)*

Figure 7 shows the characteristics of nucleation process when a groove of $w = 16.32$Å and $d = 12.24$Å is present on the substrate. Consistent with heterogeneous nucleation on flat surfaces, Figure 7(a) and (b) demonstrate that for strong interfacial interaction the bubble nucleates in the bulk while at reduced values of ε^* nucleation is observed at the interface. Pressure-time plot for $\varepsilon^* = 0.5$ shows the existence of two minimas, indicating that there exists two barriers to nucleation; this is discussed in the next Subsection. While reporting nucleation pressures, σ_{min}, in Figure 7(c) we use the minimum σ_{min} obtained in the pressure-time curves as overcoming both barriers are essential for nucleating a stable bubble. Variation of nucleation pressure with interfacial interaction shows similar behavior as compared to the cases when groove is absent (see Figure 7(d)). Unsurprisingly, for high values of ε^*, the nucleation pressure is comparable to the bulk values whereas for low ε^*, nucleation is easier when a groove is present.

2. *Effect of grooves and their geometries*

Having established that nucleation is easier on surfaces with defects when the surface does not strongly interact with the fluid, we now investigate how the groove width affects nucleation pressure in the low interaction limit. To nullify any potential effect of periodic BCs, we use a large

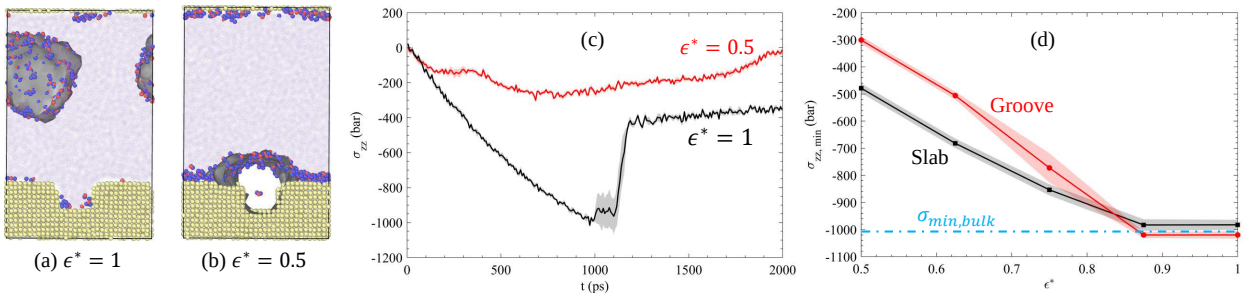

FIG. 7: Heterogeneous nucleation from surfaces with defects. (a)-(b): Strong (hydrophilic) and weak (hydrophobic) interfacial interactions (c): Pressure- time curves (d) Variation of nucleation pressure with interaction strength.

simulation box as described in the third row of Table I. The depth of groove is fixed at 12.24Å while exploring the effect of width. Our results indicate that nucleation is a two stage process, as shown in Figure 8(a). Stage 1, corresponds to the barrier associated with groove dewetting. After the system crosses Stage 1 barrier, there is a brief period where the slope of pressure-time plot is negative, indicating that the system can sustain the applied strain. Subsequently, the curve reaches another minimum and the Stage 2 barrier is reached. This second barrier is associated with the expansion of vapor and formation of the bubble beyond groove dimensions. Beyond Stage 2, the system relaxes with applied strain and the pressure-time plot acquires a positive slope. In Figure 8(b), the two barriers are shown explicitly. For small groove widths, less than $\sim$ 15Å, a stable bubble nucleated in the groove at very low strains, which is evidenced by high $\sigma_{min,Stage1}$ ($\sim$zero). With increasing groove widths, this barrier increases ($\sigma_{min,Stage1}$ reduces) as vertical walls of the groove can no longer expel out water easily. When the groove size is large, greater than 50Å, the stage 1 barrier approaches a limiting value of about -380bar, which signifies the barrier to nucleate from a step (see Supplementary Section II). Stage 2 barrier reduces ($\sigma_{min,Stage2}$ increases) with groove size, as larger the bubble formed in Stage 1, the easier it is to pull it out of the groove. Actual nucleation barrier, the minimum of Stage 1 and Stage 2, is shown in Figure 8(c); a clear reduction of barrier is observed at $\sim$20Å. This behavior could be explained based on the fact that critical nucleus radius for homogeneous nucleation was $\sim$10Å (as discussed in Section III A and Supplementary Section I); the correspondence of these two length scales leads to the maxima in Figure 8(c). Free energy calculations are necessary to further corroborate these assertions; investigations in such directions will be undertaken in the future.

To determine the effect of groove depth on nucleations pressure, we perform limited explo-

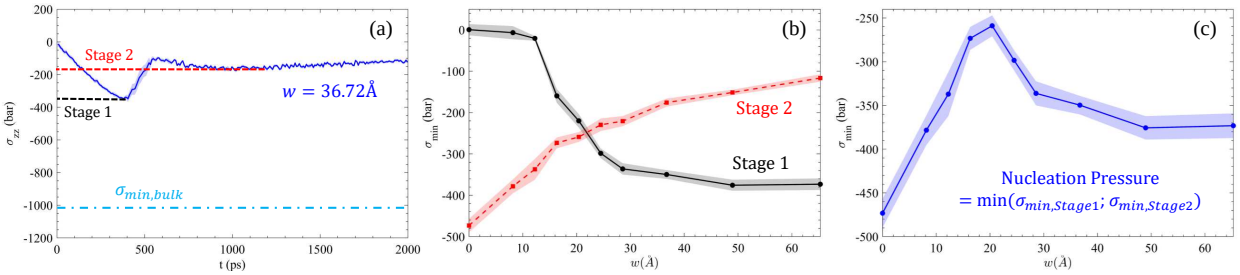

FIG. 8: (a): Two stages associated with the nucleation process from grooves (b): Nucleation pressures associated with the two stages (pressure at two local minimas in pressure-time curves) as a function of groove width (c): Minimum of stage 1 and stage 2 nucleation pressures.

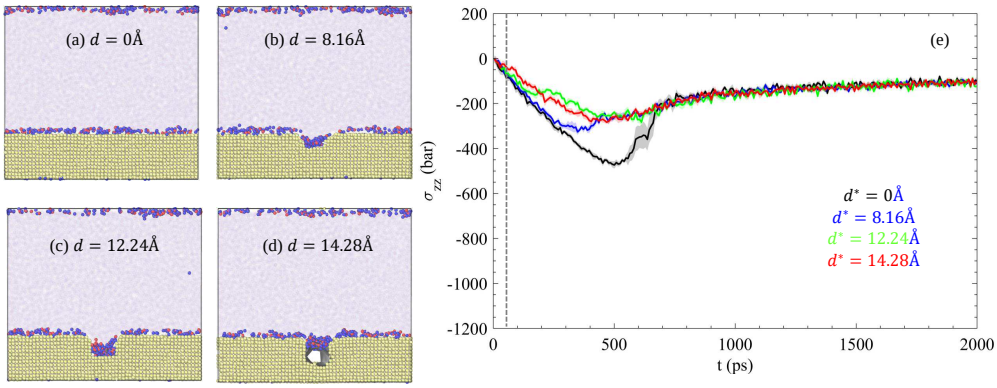

FIG. 9: Effect of groove depth on nucleation at a groove width of 16.32Å. (a)-(d): Snapshots of systems with different depths at an early stage of the nucleation process. (e): Pressure-time curves.

rations at a groove width of 16.32Å. Figure 9(a) - (d), shows snapshot of the systems with various groove depths at initial stages straining. As the depth increases, a cavity is more easily formed but it does not affect the nucleation pressure, minimum of $|\sigma_{min,Stage1}|$ and $|\sigma_{min,Stage2}|$. Therefore, as demonstrated by the pressure-time curves in Figure 9(e), Nucleation pressure reduces with increasing depth and reaches at constant value at $\sim$12.24Å. Studies at other depths are not currently explored but trends observed here are expected to hold. Extensive parametric investigations of groove dimensions (width and height) would shed more light on the exact variation of nucleation pressure.

IV. SUMMARY AND CONCLUSION

Here, we investigate homogeneous and heterogeneous bubble nucleation processes in systems under tension using molecular dynamics simulations. Advantages of studying bubble nucleation in systems under negative pressures are three fold: (a) The nucleation barrier is lowered and nucleation event can be observed within timescales accessible by MD simulations (b) Critical bubble radius is $\sim$nm, which are typical length scales attainable by MD (c) Circumvents inconsistencies – hydrophilic surfaces reduce nucleation barrier[43] as compared to hydrophobic ones – which crop up as the solid is rapidly heated to reduce the nucleation barrier. Subsequently, the maximum negative pressure sustained by the system is used a as measure of the system's propensity to nucleate a bubble.

When a system containing bulk liquid water undergoes homogeneous nucleation under negative pressures, σ_{min} approximately 1000bar and is comparable to values reported in literature[65–68]. In presence of a planar substrate, σ_{min} is comparable to homogeneous values when strong interaction exists between the gold atoms and water molecules, i.e., ε^* is large; at weaker interactions significant lowering of σ_{min} is observed, signifying that nucleation from such surfaces are easier. Reduction in σ_{min} with decreasing ε^* obtained from our simulations show a good qualitative agreement with classical heterogeneous nucleation theory.

As compared to planar surfaces, surfaces with defects show a reduction in nucleation barrier only at low ε^*, i.e., weak interfacial interactions. Furthermore, the defect geometry also influences the σ_{min}. For certain geometries of the groove there is a reduction in σ_{min}; we speculate that this occurs when the length scale of the defect is comparable to that of the critical bubble nucleation radius. Moreover, in presence of defects, multiple barriers to nucleation exist.

Overall, our results shed light on how a bubble nucleates from a atomistically flat and surfaces with defects. Future investigations on other defect geometries, air-filled grooves, free energy calculations will shed more light on the fundamental mechanisms associated with the nucleation process.

ACKNOWLEDGMENTS

This work was supported by the Office of Naval Research Thermal Science Program, Award No. N00014-17-1-2767.

AVAILABILITY OF DATA

The data that support the findings of this study are available from the corresponding author upon reasonable request.

REFERENCES

REFERENCES

[1]W. Fu, X. Li, X. Wu, and Z. Zhang, "Investigation of a long term passive cooling system using two-phase thermosyphon loops for the nuclear reactor spent fuel pool," Annals of Nuclear Energy **85**, 346–356 (2015).

[2]S. S. Murshed and C. N. De Castro, "A critical review of traditional and emerging techniques and fluids for electronics cooling," Renewable and Sustainable Energy Reviews **78**, 821–833 (2017).

[3]D. F. Hanks, Z. Lu, J. Sircar, T. R. Salamon, D. S. Antao, K. R. Bagnall, B. Barabadi, and E. N. Wang, "Nanoporous membrane device for ultra high heat flux thermal management," Microsystems & nanoengineering **4**, 1–10 (2018).

[4]H. M. Qiblawey and F. Banat, "Solar thermal desalination technologies," Desalination **220**, 633–644 (2008).

[5]D. Mills, "Advances in solar thermal electricity technology," Solar energy **76**, 19–31 (2004).

[6]O. Neumann, C. Feronti, A. D. Neumann, A. Dong, K. Schell, B. Lu, E. Kim, M. Quinn, S. Thompson, N. Grady, *et al.*, "Compact solar autoclave based on steam generation using broadband light-harvesting nanoparticles," Proceedings of the National Academy of Sciences **110**, 11677–11681 (2013).

[7]L. Zhao, B. Bhatia, L. Zhang, E. Strobach, A. Leroy, M. K. Yadav, S. Yang, T. A. Cooper, L. A. Weinstein, A. Modi, *et al.*, "A passive high-temperature high-pressure solar steam generator for medical sterilization," Joule **4**, 2733–2745 (2020).

[8]P. De Man, B. Van Straten, J. Van den Dobbelsteen, A. Van Der Eijk, T. Horeman, and H. Koeleman, "Sterilization of disposable face masks by means of standardized dry and steam sterilization processes; an alternative in the fight against mask shortages due to covid-19," Journal of Hospital Infection **105**, 356–357 (2020).

[9]J. C. Rubio-Romero, M. del Carmen Pardo-Ferreira, J. A. Torrecilla-García, and S. Calero-Castro, "Disposable masks: Disinfection and sterilization for reuse, and non-certified manufacturing, in the face of shortages during the covid-19 pandemic," Safety science **129**, 104830 (2020).

[10]P. Tao, G. Ni, C. Song, W. Shang, J. Wu, J. Zhu, G. Chen, and T. Deng, "Solar-driven interfacial evaporation," Nature energy , 1 (2018).

[11]L. Zhang, Z. Xu, B. Bhatia, B. Li, L. Zhao, and E. N. Wang, "Modeling and performance analysis of high-efficiency thermally-localized multistage solar stills," Applied Energy **266**, 114864 (2020).

[12]A. K. Menon, I. Haechler, S. Kaur, S. Lubner, and R. S. Prasher, "Enhanced solar evaporation using a photo-thermal umbrella for wastewater management," Nature Sustainability **3**, 144–151 (2020).

[13]H. Ghasemi, G. Ni, A. M. Marconnet, J. Loomis, S. Yerci, N. Miljkovic, and G. Chen, "Solar steam generation by heat localization," Nature communications **5**, 1–7 (2014).

[14]A. H. Persad and C. A. Ward, "Expressions for the evaporation and condensation coefficients in the hertz-knudsen relation," Chemical reviews **116**, 7727–7767 (2016).

[15]S.-p. Guo, Z. Wu, W. Li, D. Kukulka, B. Sundén, X.-p. Zhou, J.-j. Wei, and T. Simon, "Condensation and evaporation heat transfer characteristics in horizontal smooth, herringbone and enhanced surface eht tubes," International Journal of Heat and Mass Transfer **85**, 281–291 (2015).

[16]A. Chandra, *Interfacial Relations in Liquid-Vapor Phase Change Processes: An Atomistic and Continuum Study* (Rensselaer Polytechnic Institute, 2021).

[17]A. Rokoni and Y. Sun, "Probing the temperature profile across a liquid–vapor interface upon phase change," The Journal of Chemical Physics **153**, 144706 (2020).

[18]A. Chandra and P. Keblinski, "Investigating the validity of schrage relationships for water using molecular dynamics simulations," The Journal of Chemical Physics **153**, 124505 (2020).

[19]Z. Liang, T. Biben, and P. Keblinski, "Molecular simulation of steady-state evaporation and condensation: Validity of the schrage relationships," International Journal of Heat and Mass Transfer **114**, 105–114 (2017).

[20]Z. Liang, A. Chandra, E. Bird, and P. Keblinski, "A molecular dynamics study of transient evaporation and condensation," International Journal of Heat and Mass Transfer **149**, 119152 (2020).

[21]F. Yang, A. Chandra, Y. Zhang, S. Tendulkar, R. Nastasia, A. A. Oberai, M. S. Shephard, and O. Sahni, "A parallel interface tracking approach for evolving geometry problems," Engineering with Computers **38**, 4289–4305 (2022).

[22]Y. Zhang, A. Chandra, F. Yang, E. Shams, O. Sahni, M. Shephard, and A. A. Oberai, "A locally discontinuous ale finite element formulation for compressible phase change problems," Journal of Computational Physics **393**, 438–464 (2019).

[23]A. Chandra, Z. Liang, A. A. Oberai, O. Sahni, and P. Keblinski, "On the applicability of continuum scale models for ultrafast nanoscale liquid-vapor phase change," International Journal of Multiphase Flow **135**, 103508 (2021).

[24]A. Chandra, P. Keblinski, O. Sahni, and A. A. Oberai, "A continuum framework for modeling liquid-vapor interfaces out of local thermal equilibrium," International Journal of Heat and Mass Transfer **144**, 118597 (2019).

[25]K. Engelberg-Forster and R. Greif, "Heat transfer to a boiling liquid—mechanism and correlations," Journal of Heat Transfer **81**, 43–52 (1959).

[26]P. A. Kew and K. Cornwell, "Correlations for the prediction of boiling heat transfer in small-diameter channels," Applied thermal engineering **17**, 705–715 (1997).

[27]F. Caupin and E. Herbert, "Cavitation in water: a review," Comptes Rendus Physique **7**, 1000–1017 (2006).

[28]B. M. Borkent, S. Gekle, A. Prosperetti, and D. Lohse, "Nucleation threshold and deactivation mechanisms of nanoscopic cavitation nuclei," Physics of fluids **21**, 102003 (2009).

[29]V. K. Shen and P. G. Debenedetti, "A computational study of homogeneous liquid–vapor nucleation in the lennard-jones fluid," The Journal of chemical physics **111**, 3581–3589 (1999).

[30]S. L. Meadley and F. A. Escobedo, "Thermodynamics and kinetics of bubble nucleation: Simulation methodology," The Journal of chemical physics **137**, 074109 (2012).

[31]J. Nie, A. Chandra, Z. Liang, and P. Keblinski, "Mass accommodation at a high-velocity water liquid-vapor interface," The Journal of chemical physics **150** (2019).

[32]G. Menzl, M. A. Gonzalez, P. Geiger, F. Caupin, J. L. Abascal, C. Valeriani, and C. Dellago, "Molecular mechanism for cavitation in water under tension," Proceedings of the National Academy of Sciences **113**, 13582–13587 (2016).

[33]Y. Wang, X. Li, S. Ren, H. T. Alem, L. Yang, and D. Lohse, "Entrapment of interfacial nanobubbles on nano-structured surfaces," Soft matter **13**, 5381–5388 (2017).

[34]A. Bussonnière, Q. Liu, and P. A. Tsai, "Cavitation nuclei regeneration in a water-particle suspension," Physical review letters **124**, 034501 (2020).

[35]S. Xie, M. S. Beni, J. Cai, and J. Zhao, "Review of critical-heat-flux enhancement methods," International Journal of Heat and Mass Transfer **122**, 275–289 (2018).

[36]K.-H. Chu, Y. Soo Joung, R. Enright, C. R. Buie, and E. N. Wang, "Hierarchically structured surfaces for boiling critical heat flux enhancement," Applied Physics Letters **102**, 151602 (2013).

[37]C. Li, Z. Wang, P.-I. Wang, Y. Peles, N. Koratkar, and G. Peterson, "Nanostructured copper interfaces for enhanced boiling," small **4**, 1084–1088 (2008).

[38]X. Dai, F. Yang, R. Yang, X. Huang, W. A. Rigdon, X. Li, and C. Li, "Biphilic nanoporous surfaces enabled exceptional drag reduction and capillary evaporation enhancement," Applied Physics Letters **105**, 191611 (2014).

[39]A. Zou and S. C. Maroo, "Critical height of micro/nano structures for pool boiling heat transfer enhancement," Applied Physics Letters **103**, 221602 (2013).

[40]K.-H. Chu, R. Enright, and E. N. Wang, "Structured surfaces for enhanced pool boiling heat transfer," Applied Physics Letters **100**, 241603 (2012).

[41]R. W. Schrage, *A theoretical study of interphase mass transfer* (Columbia University Press, 1953).

[42]T. Yamamoto and M. Matsumoto, "Initial stage of nucleate boiling: molecular dynamics investigation," Journal of Thermal Science and Technology **7**, 334–349 (2012).

[43]S. M. Shavik, M. N. Hasan, A. M. Morshed, and M. Q. Islam, "Molecular dynamics study of effect of different wetting conditions on evaporation and rapid boiling of ultra–thin argon layer over platinum surface," Procedia Engineering **105**, 446–451 (2015).

[44]K. Sasikumar, Z. Liang, D. G. Cahill, and P. Keblinski, "Curvature induced phase stability of an intensely heated liquid," The Journal of chemical physics **140**, 234506 (2014).

[45]S. Twomey, "Experimental test of the volmer theory of heterogeneous nucleation," The Journal of Chemical Physics **30**, 941–943 (1959).

[46]S. Maruyama, T. Kimura, and Y. Yamaguchi, "A molecular dynamics simulation of a bubble nucleation on solid surface," in *National Heat Transfer Symposium of Japan*, Vol. 34 (Citeseer, 1997) pp. 675–676.

[47]Wu, "A molecular dynamics simulation of bubble nucleation in homogeneous liquid under heating with constant mean negative pressure," Microscale Thermophysical Engineering **7**, 137–151 (2003).

[48]S. Plimpton, "Fast parallel algorithms for short-range molecular dynamics," Journal of Computational Physics **117**, 1 – 19 (1995).

[49]A. Stukowski, "Visualization and analysis of atomistic simulation data with OVITO-the Open Visualization Tool," MODELLING AND SIMULATION IN MATERIALS SCIENCE AND ENGINEERING **18** (2010), 10.1088/0965-0393/18/1/015012.

[50]H. J. C. Berendsen, J. R. Grigera, and T. P. Straatsma, "The missing term in effective pair potentials," The Journal of Physical Chemistry **91**, 6269–6271 (1987), ttps://doi.org/10.1021/j100308a038.

[51]D. Wolf, P. Keblinski, S. Phillpot, and J. Eggebrecht, "Exact method for the simulation of coulombic systems by spherically truncated, pairwise r- 1 summation," The Journal of chemical physics **110**, 8254–8282 (1999).

[52]F. N. Mendoza, J. López-Lemus, G. A. Chapela, and J. Alejandre, "The wolf method applied to the liquid-vapor interface of water," The Journal of chemical physics **129**, 024706 (2008).

[53]J.-P. Ryckaert, G. Ciccotti, and H. J. Berendsen, "Numerical integration of the cartesian equations of motion of a system with constraints: molecular dynamics of n-alkanes," Journal of computational physics **23**, 327–341 (1977).

[54]S. Foiles, M. Baskes, and M. S. Daw, "Embedded-atom-method functions for the fcc metals cu, ag, au, ni, pd, pt, and their alloys," Physical review B **33**, 7983 (1986).

[55]S. Merabia, S. Shenogin, L. Joly, P. Keblinski, and J.-L. Barrat, "Heat transfer from nanoparticles: A corresponding state analysis," Proceedings of the National Academy of Sciences **106**, 15113–15118 (2009).

[56]W. Shinoda, M. Shiga, and M. Mikami, "Rapid estimation of elastic constants by molecular dynamics simulation under constant stress," Physical Review B **69**, 134103 (2004).

[57]M. E. Tuckerman, J. Alejandre, R. López-Rendón, A. L. Jochim, and G. J. Martyna, "A liouville-operator derived measure-preserving integrator for molecular dynamics simulations in the isothermal–isobaric ensemble," Journal of Physics A: Mathematical and General **39**, 5629 (2006).

[58]M. Parrinello and A. Rahman, "Polymorphic transitions in single crystals: A new molecular dynamics method," Journal of Applied physics **52**, 7182–7190 (1981).

[59]G. J. Martyna, D. J. Tobias, and M. L. Klein, "Constant pressure molecular dynamics algorithms," The Journal of chemical physics **101**, 4177–4189 (1994).

[60]W. G. Hoover, "Canonical dynamics: Equilibrium phase-space distributions," Physical review A **31**, 1695 (1985).

[61]S. Nosé, "A unified formulation of the constant temperature molecular dynamics methods," The Journal of chemical physics **81**, 511–519 (1984).

[62]S. Nosé, "A unified formulation of the constant temperature molecular dynamics methods," The Journal of chemical physics **81**, 511–519 (1984).

[63]W. G. Hoover, "Canonical dynamics: Equilibrium phase-space distributions," Physical review A **31**, 1695 (1985).

[64]H. Jiang and A. J. Patel, "Recent advances in estimating contact angles using molecular simulations and enhanced sampling methods," Current Opinion in Chemical Engineering **23**, 130–137 (2019).

[65]J. C. Fisher, "The fracture of liquids," Journal of applied Physics **19**, 1062–1067 (1948).

[66]P. G. Debenedetti, *Metastable liquids: concepts and principles*, Vol. 1 (Princeton university press, 1996).

[67]M. E. M. Azouzi, C. Ramboz, J.-F. Lenain, and F. Caupin, "A coherent picture of water at extreme negative pressure," Nature Physics **9**, 38–41 (2013).

[68]F. Caupin, "Liquid-vapor interface, cavitation, and the phase diagram of water," Physical Review E **71**, 051605 (2005).

[69]H. J. Maris, "Introduction to the physics of nucleation," Comptes Rendus Physique **7**, 946–958 (2006).

[70]N. Shenogina, R. Godawat, P. Keblinski, and S. Garde, "How wetting and adhesion affect thermal conductance of a range of hydrophobic to hydrophilic aqueous interfaces," Physical review letters **102**, 156101 (2009).

SUPPLEMENTARY INFORMATION

Nucleus size

To estimate the critical bubble radius in homogeneous nucleation process, OVITO's construct Surface mesh feature is used to estimate the volume and surface area of the vapor cavity formed. Assuming the cavity is a spherical, the radius is estimated. As shown in Figure 10, in all the three simulation box sizes considered, the radius is approximately 10Å. The bubble radius where the

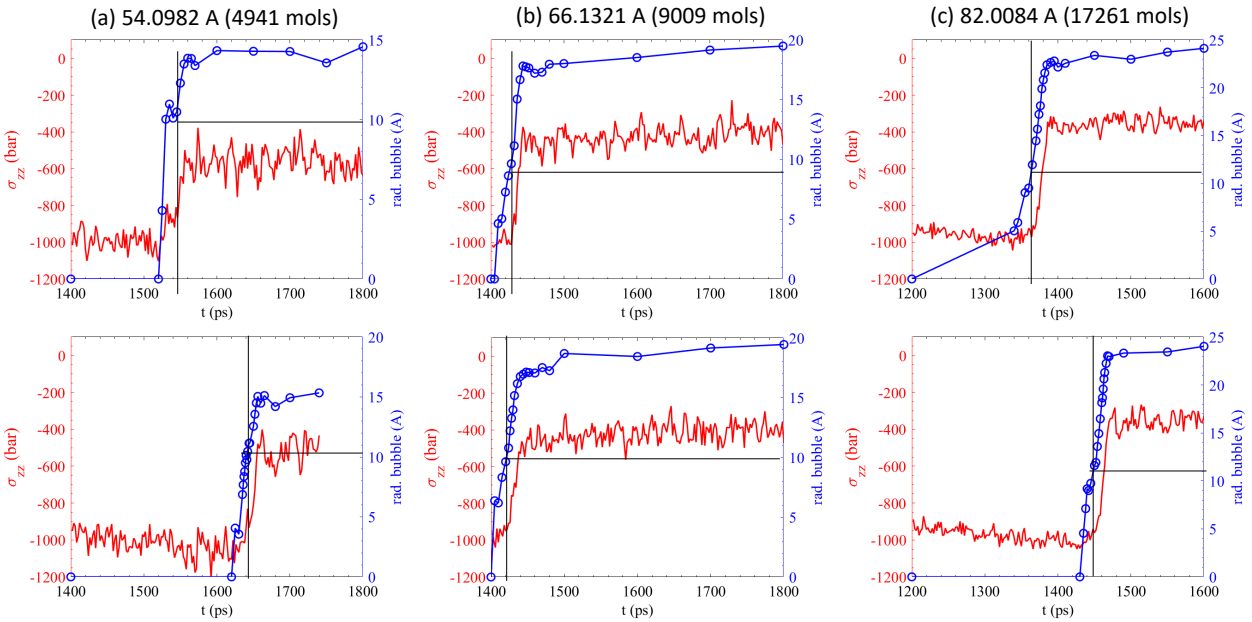

FIG. 10: Critical bubble size obtained in homogeneous nucleation for three simulation box sizes (a)-(c). The columns represent two independent runs for each box size.

pressure starts increasing is defined as the critical bubble radius.

Effect of groove width

Figure 11 shows the Pressure time curves for different groove widths. At w=12.24Å, Stage 1 is almost non-existent – small negative value at t=0ps. At w=20.4Å, the two stages are clearly visible ($t \sim 200ps$ and $t \sim 600ps$). Finally, at w=65.28Å, multiple sub-stages exist, but the two local minimas are prominent ($t \sim 450ps$ and $t \sim 2000ps$). As the system is strained, the bubble first nucleates from one edge of the groove, grows and attaches to the other edge of the groove, grows out of the groove, and finally overcomes the Stage 2 barrier.

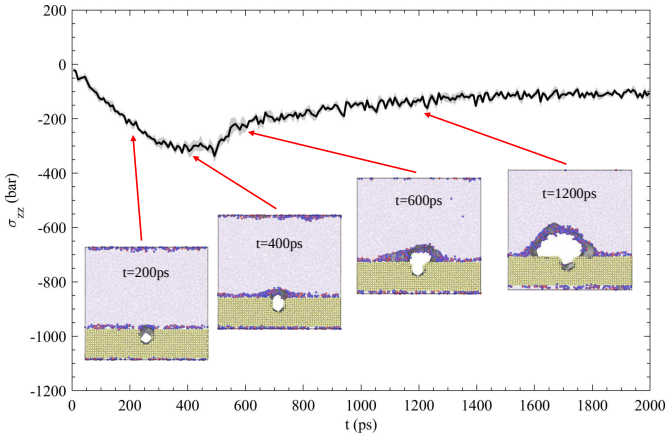

(a) w=12.24Å

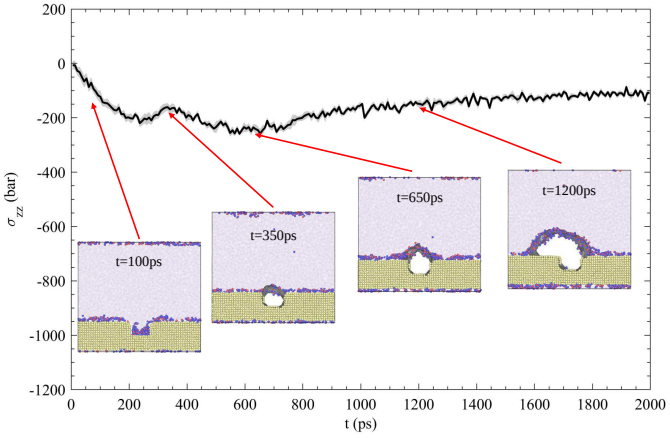

(b) w=20.4Å

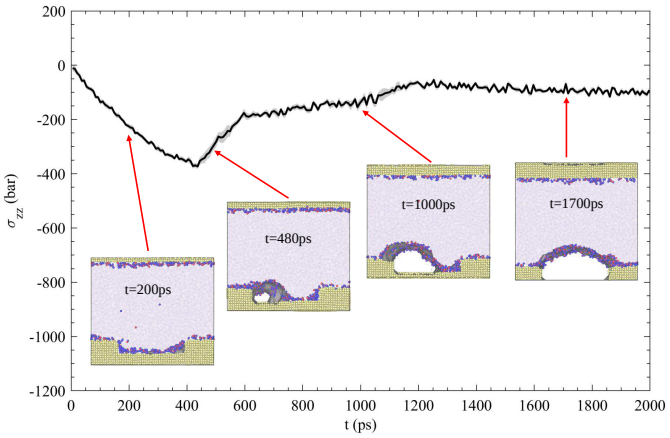

(c) w=65.28Å

FIG. 11: Pressure-time curves for different groove widths at a fixed depth of 12.24Å.